Egyptian Geophysical Society
EGS Journal, Vol. 17, No. 1, 139-154 (2019)

BUILDING BASEMENT STRUCTURE MODELS USING SATELLITE GRAVITY DATA IN SOUTHWESTERN EGYPT

A.S. HELALY
Department of Geophysics, Faculty of Science, Ain Sham University
Abbassiah, Cairo, Egypt.

بناء نماذج تركيبية لصخور القاعدة باستخدام بيانات الجاذبية غير الأرضية فى جنوب غرب مصر

الخلاصة: تم تطبيق بعض تقنيات تحسين البيانات على بيانات الجاذبية غير الأرضية في منطقة العوينات والمناطق المجاورة ، جنوب غرب مصر. تم تنفيذ هذه التقنيات من خلال تحليل مجال التردد بواسطة تحويل فورير ثنائي الأبعاد لمنحنيات التثاقلية المأخوذة من خريطة الجاذبية المتبقية التي تم تحليلها لبناء نماذج البنية الإقليمية لصخور القاعدة. تم الكشف عن عناصر تركيبية رئيسية على طول النماذج المدروسة التي تؤثر في صخور القاعدة تحت السطحية والغطاء الرسوبي المغطي. تظهر هذه التراكيب بعض التموجات المتغايرة في الجاذبية. ووجد أن نمط الصدع يتسبب في تشكيل إرتفاعات متغيرة ومتناوبة مع إنخفاضات (أحواض) في الامتدادات المساحية المتغيرة في الصخورالقاعدة. تشكل بعض الإنخفاضات الفرعية إحتمالات أن تكون مناسبة كأحواض لتجمعات المياه الجوفية في منطقة الدراسة. الإنخفاض العام لسطح القاع يلاحظ باتجاه الشمال والشرق والشمال الشرقي.

ABSTRACT: *Some data enhancement techniques were applied on satellite gravity data in Oweinat and nearby areas, southwestern Egypt. These techniques were performed in the frequency-domain accomplished by a 2-D Fourier-Transformation of the residual profiles taken from the median-filtered residual gravity map for building regional basement structure models. Major fault elements were detected along the studied profiles that dissect the subsurface basement rocks and their overlying sedimentary cover. These faults appear with different fault patterns which are responsible for gravity anomaly undulations. The fault pattern causes the formation of alternating swells and troughs of variable areal extensions in basement rocks. Some troughs form sub-basins that could be suitable for groundwater accumulations basins in the study area. The general dip of the basement surface is towards the north, east and northeastern directions.*

INTRODUCTION

The structural analysis of the basement rocks can advance the understanding of the overlying structures and the petroleum system in any study area, and the study of the basement structures not only benefits the investigation of tectonic structures, but also helps to detect and explore the probable contained mineral resources (Alexander et al., 2003). Aeromagnetic and gravity surveys are necessary to establish the depth and shape of the basement rocks beneath the sediments in the southern part of the Western Desert. This knowledge is essential to a full understanding of the underground water reservoir and its future (El-Baz, et al; 1978).

The study area lies at the southwestern part of Egypt. It is bounded by latitudes 22º 00' N & 24º 30' N and longitudes 25º 00' E & 30º 00' E and covers a surface area of about 125,000 km^2 as shown in Figure (1). The study area is of a sedimentary terrain, ranging in age from Precambrian to Quaternary, but with many missing ages in between. It is an arid region with a few drainage lines which are draining eastward in general.

The main goal of this work is to recognize the subsurface basement relief and structures affecting the basement complex and its overlying sedimentary cover.

Interpretation of the gravity anomaly map and concluding the probable existed geological structural features prevailing in the study area were carried out. This gravity map was filtered using some different techniques. Also, the Geosoft and Surfer (version 13) programs have been used for carrying out the required analytical operations using the available map data sets.

The study area belongs to Al-Wadi Al-Jadid Governorate within the Western Desert. In general, it is considered as a huge platform of sedimentary sequence that is thinning southward while thickening northward. The general higher topography (from, Helaly, 2018) is towards the West, while becoming of lower terrain towards the East as shown in topographic 3D view (Figure 2).

Most of the sedimentary rock units composing the Western Desert are dipping smoothly northward. In general, the Western Desert is dominated by the Nubian Sandstone rocks at the south, Cretaceous- Eocene Limestone rocks in the middle, and Miocene Limestones towards the north. The eastern side of the Western Desert is characterized by relative smaller thicknesses of sedimentary rocks due to the effect of faulting and folding. Structurally, the Western Desert shows some folding features in the subsurface, which could be divided into three major groups (Said, 1962): N-S folding, NE-SW folding, and, NW-SE folding.

Structural Setting

The general flatness of the southwestern desert of Egypt is its most striking feature (Figure 3). Rock beds are nearly horizontal, and only in rare cases significant angles of dip can be noticed, e.g., at Karkur Talh (Oweinat), where several short E-W faults exist. The main faults in this part of the desert are normal gravity faults, including the Gilf fault, which extends about 150 km in a NNE direction on the west side of the Gilf Kebir; the Kemal fault, which is also 150 km long and trends in

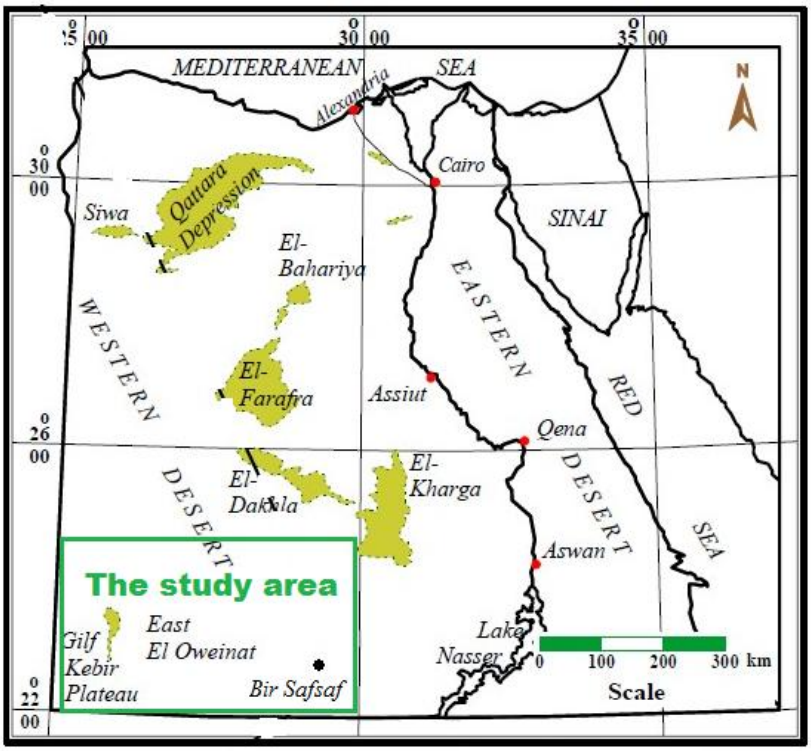

Figure (1): Location map of the study area.

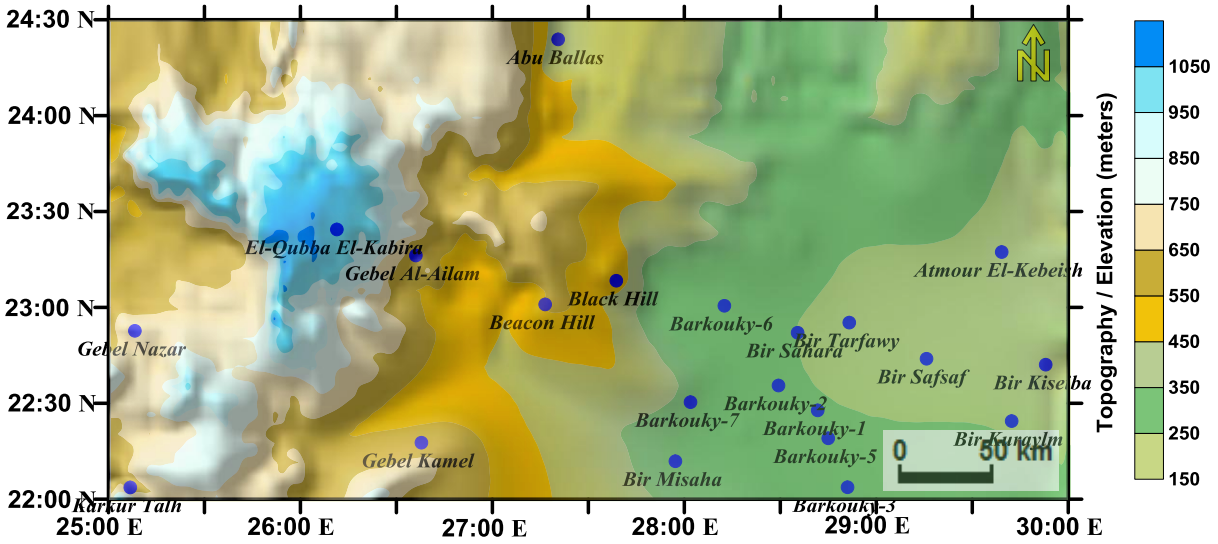

Figure 2: The topographic map showing popular localities.

a NW direction along the western Gilf; and the Tarfawi fault, which skirts the western side of the Tarfawi igneous mass and runs over 220 km in a NNE direction. The distribution of the basement rocks, and the type and thickness of sediments, reflect several phases of structural development. Of importance are the two main igneous bodies at Oweinat in the west and Tarfawi in the east. Between these two main masses lies the thick clastic section of the Gilf Sandstone indicating a basin of significant depth and continuation.

The Lower Palaeozoic sediments are poorly represented in the Oweinat area, while the Devonian-Carboniferous are better developed and show evidences of being slightly folded. This folding and the igneous intrusions may indicate post-Carboniferous orogenic movements that resulted in the Oweinat high. The configuration of the Gilf basin is bounded eastward by the Tarfawi high. Because the sediments within the Tarfawi high are mostly Cretaceous and younger, it appears that the rise of the basement was initiated during a much later date than that of the Oweinat high.

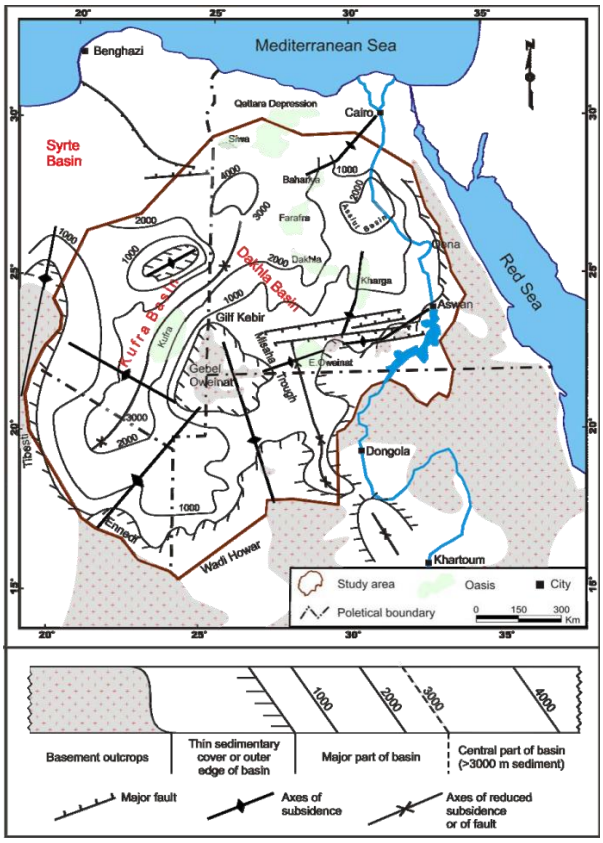

Figure 3: General structural framework of the NSAS, adapted from Klitzsch (1984), Klitzsch and Wycisk (1989)

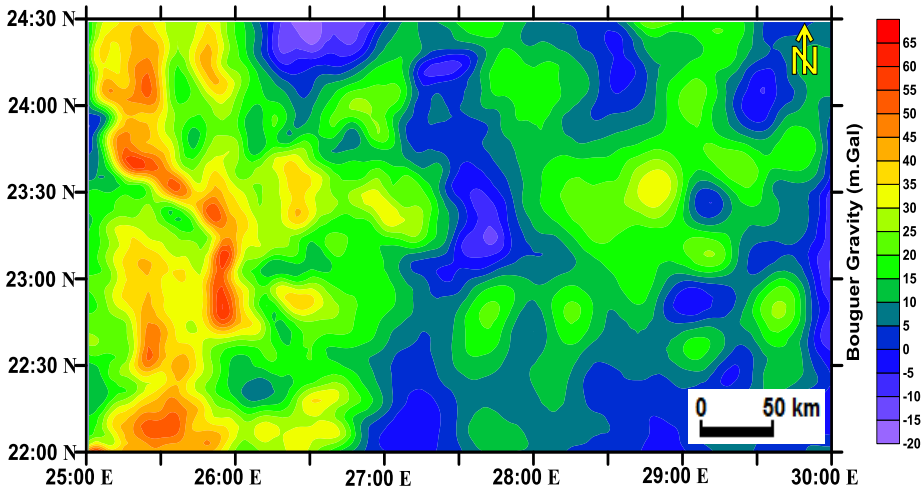

Figure 4: Bouguer anomaly gravity map. (C.I.=5 m.Gal)

The only igneous rocks associated with this later movement are basalts of Cretaceous-Oligocene age. Northward extrapolation of these highs and lows makes it obvious that the Tarfawi high trends north-northeast to join the Kharga swell. The Gilf basin, which assumes nearly the same trend, is believed to be a southern extension of the Dakhla basin, while the Oweinat high, also of the same trend, is mantled by the thick cover of the Great Sand Sea to the north. The fact that the western part of the area had been very active during the Late Palaeozoic-Early Mesozoic whereas the eastern part shows signs of being unstable during the Cretaceous and Early Tertiary points to an eastward shift of tectonism with time **(**Burollet, 1963 and El-Baz et al, 1978).

AVAILABLE DATA

Bouguer gravity anomaly map (Figure 4) was obtained from the work of Helaly (2018) and used for

analysis of the present work. Bouguer gravity anomaly shows several anomalous features of varying trends and amplitudes. In general, higher gravity values range from 15 m.Galup to slightly higher than 45 m.Gal are within the western half of the gravity map, while lower gravity values range from less than 0 m.Galup to about 25 m.Gal within the eastern half. The high NW elongated trend anomaly dominates which reflects the Gilf Al-Kebir structural high. There is another general N-S high anomaly. In the central part of the eastern half, the anomaly is relatively stronger than the surroundings. Obvious NE trend can be seen with some parallel highs and lows. This gives the area the characteristics of some depressions related with uplifts in the general N-S and NE-SW extending gravity high and gravity low that lie generally in parallel.

METHODOLOGY

Regional-Residual Isolation using the Polynomial Procedure

The gravity and magnetic data represent a combination of the effects from the deeper and shallower causative sources. Anomalies with long wavelength (large width) are generated by deeper sources while short wavelength anomalies are from shallower sources. Different techniques can be used for isolating the residual from the regional trend (long wavelength component). The graphical way of such isolation can be used by which, the regional background is estimated by visual inspection. The regional-residual isolation based on polynomial fitting was proposed by Beltrao (1991), in which the coefficients are determined by a strong procedure consisting of iteratively re-weighted least squares solutions. By successively assigning small weights to large residuals, their influence in the fitted regional is minimized regardless of the "true" residual anomalies signs. It is a process that is insensitive to small departure from the idealized assumptions for which the estimator is optimized.

Also, Abdelrahman et al. (2003) presented a procedure to select the optimum polynomial order, based on the correlation between residuals of successive orders. It is concluded that the success of this method depends on the accuracy with which the residual anomaly is separated from the observed gravity anomaly. The residual gravity map is important in defining the geological structures and boundaries which are targets of geophysical exploration. It is noted that, polynomial fitting (trend surface analysis) provided the best numerical approach. Therefore, it is more appropriate to compute from a gridded data, the best fit smooth surface using the least-squares polynomial fitting order and then remove the regional background (Nettleton, 1976).

The residual gravity map will be useful for the determination of the thickness of the basins and the study of the underlying basement. It will also be handy for tectonic studies, anomaly transformation and mineral exploration in the flank.

Then, using the obtained regional map, the residual map (Figure 5) is produced by subtracting the obtained regional from the total Bouguer anomaly map.

As a general investigation of the residual gravity data, a 2-D Fourier Transform Analysis was carried out over the residual gravity data shown in Figure (5) to get an idea about the overall average depth to the underlying basement rocks. It is concluded that the average depth around 0.3 km (300 meters below the Earth's surface, as deduced from Figure (6).

Further Analysis of the Residual Gravity Data

1) The residual gravity map with the dimension of five longitude degrees (from 25°:00′:00″ to 30°:00′:00″) and two and half latitude degrees (from 22°:00′:00″ to 24°:30′:00″) was subdivided into fifty (50) blocks, each of which with dimensions of half a degree (longitude) by half a degree (latitude). as shown in the layout of Figure (7).

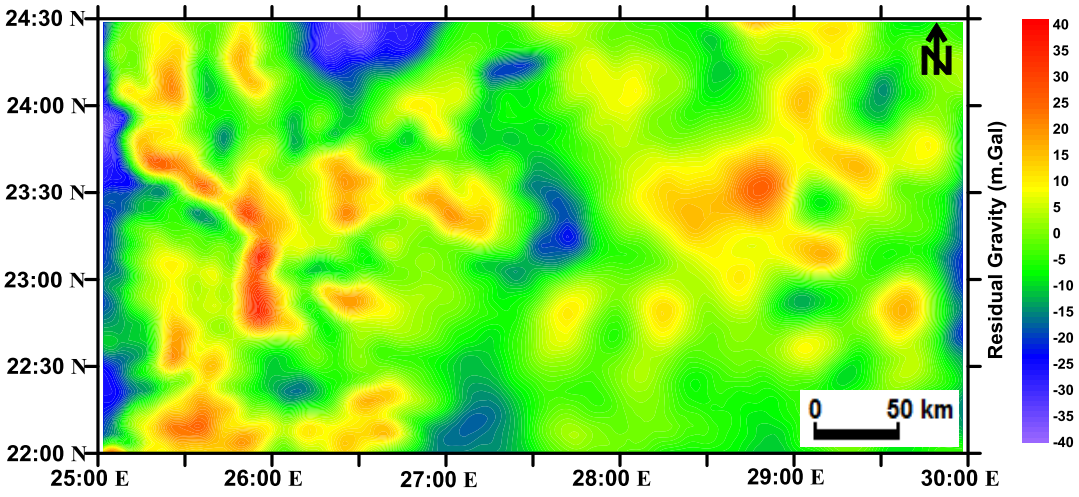

Figure (5): Residual gravity anomaly map computed by removing a second order polynomial surface (regional) from the Bouguer gravity anomaly map. (C.I.= 1 m.Gal).

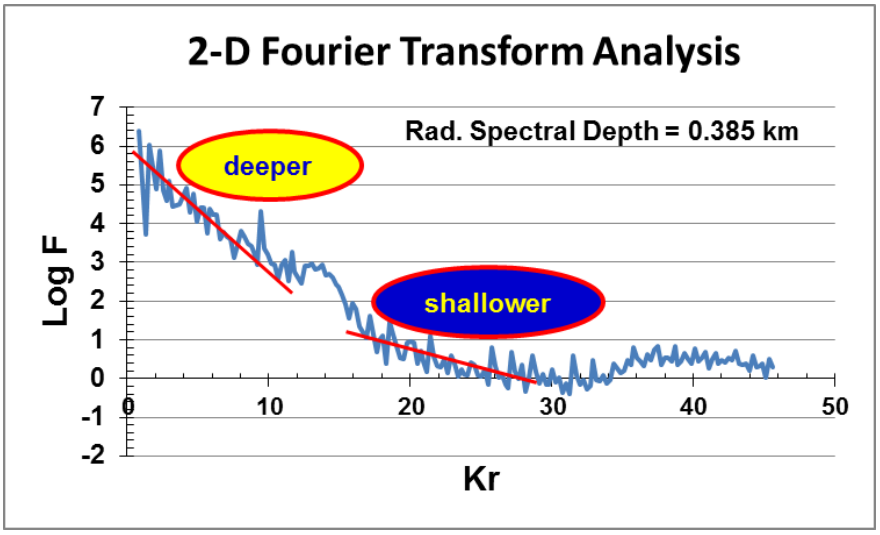

Figure (6): Radially Averaged 2-D Spectral Analysis Curve for the whole Residual Gravity Data.

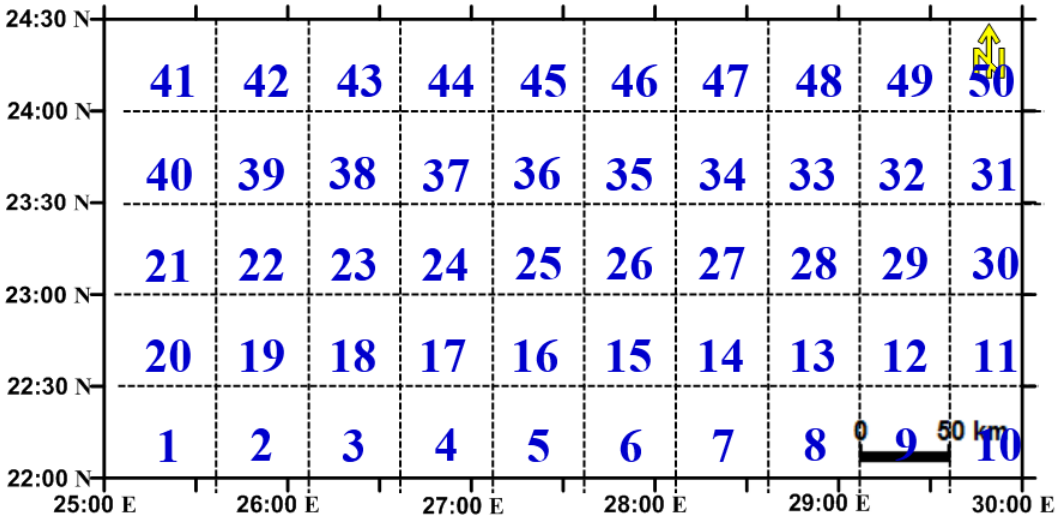

Figure (7): Distribution of blocks used in Power Spectrum Analysis.

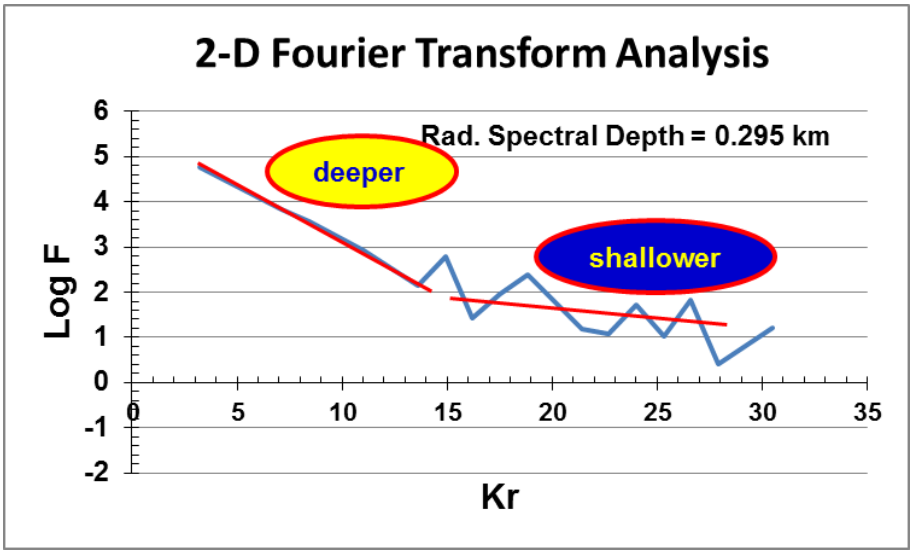

Figure (8): Radially Averaged 2-D Spectral Analysis Curve for the Residual Gravity Data in one of the blocks.

2) Each block was then analyzed using the Fourier Transform of the Power Spectrum work, as has been done in Figure (6), to determine the average basement depth within that specific block. Figure (8) shows an example of the used Power spectrum curves in this study in one of the blocks. Less number of data points was encountered in each block than the original residual map's spectrum. The estimated average depth (for each block) was then designated at each block's center point. Fifty depth-to-basement values were obtained within the whole area.
3) The fifty depth-to-basement (deep) values were then, gridded through the Kriging method, and contoured with the Surfer-13 software as shown in Figure (9) that illustrates the depth-to-basement map from the ground surface, and Figure (10) that shows the depth-to-basement map with respect to the mean sea level.

The Nubian Sandstone aquifer overlies the basement which is dissected by numerous fault systems (Issawi, 1971; Issawi, 1978) and as illustrated in (Helaly, 2018). The Nubian Sandstone system is classified to six distinct geological units ranging in age from Jurassic to Upper Cretaceous (Klitzsch et al., 1979; Klitzsch and Lejal-Nicol, 1984). But this classification can be gathered into three main integrated units; a surface cover together with a dry part of the Nubian Sandstone, water-saturated beds of the Nubian Sandstone and the basement rocks (Abd El Latif et al., 1997).

Figure (9) illustrates the general variation of the basement depths from the ground earth's surface. The depth values ranged from -50 meter to about -600 meter below the ground surface. The shallowest depths were encountered at the western and northeastern sides, which represent the majority of the study area. Three low-lying spots (basin-like) of relatively deeper depths can be seen clearly within the area. The three basins are aligned with a general northwest trend. The deepest encountered depth is within the middle basin with an interpreted depth of about -500 to -600 meters below the ground surface. El Nahry, et al (2010) through their study at the farthest south-eastern block of the current study area, they measured the depths to the basement blocks and found that the depths are ranging between about 700 meters (in the areas of deepest basement below the ground surface) to about 150 meters (in the areas of shallowest basement below the ground surface). This agrees approximately with the deduced interpreted depths from the current study. Taking into consideration that the current study is somehow more regional than the previous studies, some interpreted depths are different.

For being required in the upcoming gravity data modelling, it was needed to estimate the approximate basement depth values from the mean sea level. Figure (10) demonstrates such general variation of the basement depth from the mean sea level. As shown, the depth variations ranged from about +900 meters above the mean sea level to about -250 meter below the mean sea level. In general, the basement depths were above the mean sea level at the western and north eastern regions, while in general, the southeastern quarter of the study area shows lower basement altitudes below the mean sea level.

Gravity Data Median Filtering

The obtained residual gravity data may suffer from some errors (corrugations), which are data inconsistencies between adjacent stations arising from a variety of, in general, unavoidable acquisition-related circumstances or similar reasons. Because the coming data processing will involve the use of Fourier Transform in analyzing the studied residual gravity data, and such analysis work may be distorted and shows data redundancy, it was preferable to filter the residual gravity data for minimizing the data redundancy in the later processed results. Mauring and Kihle (2006) introduced a technique (*Median Filtering*) for smoothing the collected data along regular line pattern in aero-geophysical work. The technique involves a moving differential median filter to minimize the expected errors.

Generally, the median filter is considered as a nonlinear digital filtering technique, which can be used to remove noise from an image or signal. Such noise reduction is a typical pre-processing step to improve the results of later processing (for example, edge detection on an image or a map). Originally, median filtering is widely used in digital image processing because, under certain conditions, it preserves edges while removing noise.

The main idea of the median filter is to run through the signal entry by entry, replacing each entry with the median of neighboring entries. The pattern of neighbors is called the "window", which slides, entry by entry, over the entire signal. The median is calculated by first sorting all the pixel values from the window into numerical order, and then replacing the pixel being considered with the middle (median) pixel value.

For 1D signals, the most obvious window is just the first few preceding and following entries, whereas for 2D (or higher-dimensional) signals such as images or maps, more complex window patterns are possible (such as "box"). Usually, the window has an odd number of entries, by which the median is simple to define; it is just the middle value after all the entries in the window are sorted numerically. It replaces the value of the center pixel with the median of the intensity values in the neighborhood of that pixel. The median filter is more effective than convolution when the goal is to simultaneously reduce noise and preserve edges.

Although it is a smoothing filter, it preserves sharp edges in a data set (Gallagher and Wise, 1981; Justusson, 1981 and Stewart, 1985). Both properties are illustrated in Figure 11; which also outlines the 1D median filtering procedure. A 2D median filter is a simple extension of the 1D filter to an array of numbers contained within an area. Testing of this technique for removing unwanted signals is explained in Mauring and Kihle (2006).

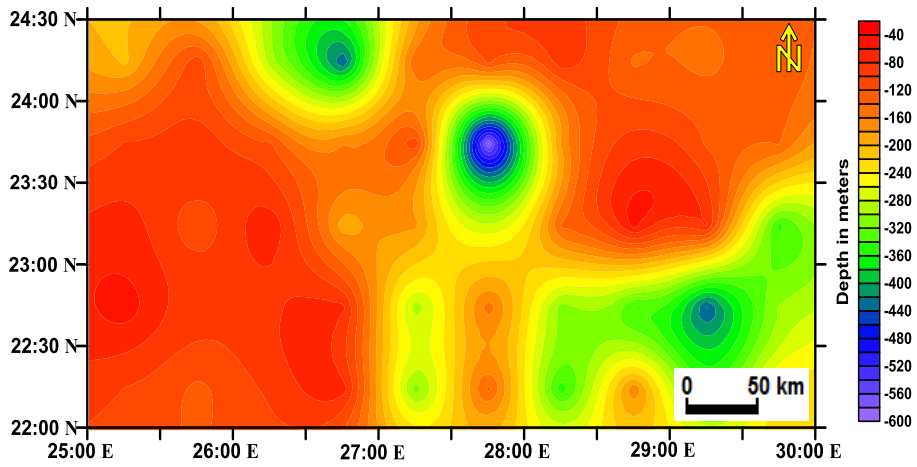

Figure (9): Basement depth map (from ground Surface Level). C.I. = 20 meters.

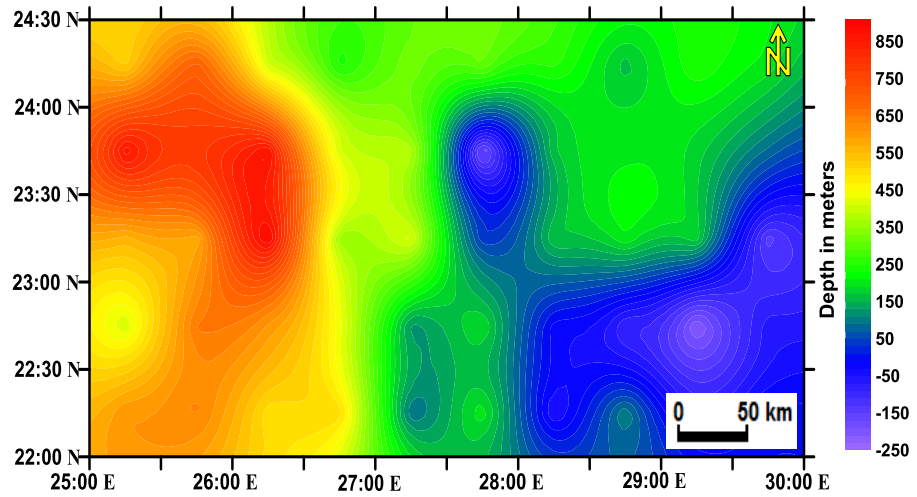

Figure (10): Basement depth map (from Sea level) C.I. = 20 meters.

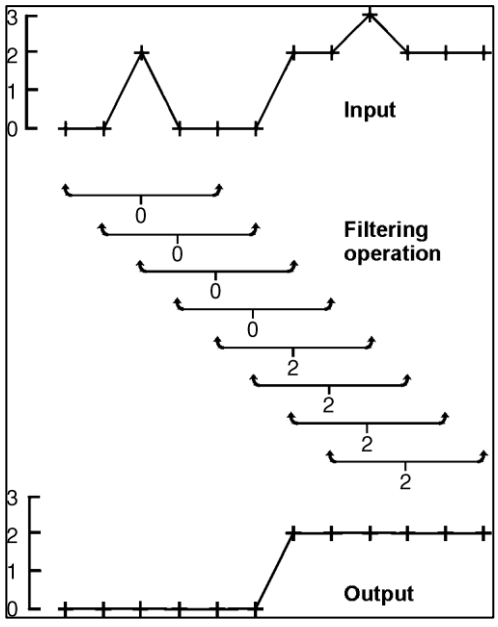

Figure (11): Procedure for the median filtering of lines using a five-point filter (after Stewart, 1985). Note the removal of spikes and the preservation of edges in the data.

The available residual gravity data usually have some unwanted signals (noise) which may cause distortion of the main wanted signals. Therefore, before performing further processing techniques, the gravity data was subjected to some sort of smoothing the data using a median filter of a moving 3x3 window. This is to smooth gridded data and to remove outliers (spikes) from it. This filter can greatly improve the results of the further Fourier Transform operations. The studied residual gravity data was converted into its median-filtered version using Median filter C++ code, as shown in the following Figure (12).

The obtained filtered map displayed in Figure (12) shows more harmony in the anomaly distribution pattern than the original residual gravity map, where the scattered short wavelength anomalies existed in Figure (5) was almost completely reduced or removed. The main and major positive and negative anomalies are better enhanced and focused on the configuration of the main subsurface causative features. This more proportioned anomaly pattern will minimize the redundancy while applying the next processing techniques. So, this filtered map was then used for further quantitative analysis along four selected profiles 'directions within the study area as shown Figure (12). These profiles directions were chosen along some imperative anomalies to uncover the general setup of the subsurface relief of the basement rock and the overlying sedimentary section. Therefore, the main objective of the following work was to apply such different techniques on the gravity data to identify possible faults and their physical locations within the study area. This is followed by modeling the subsurface setup using the deduced basement depth (from Figures 8 and 9) and the detected dissecting fault elements that are shaping the basement surface and affecting the overlying sedimentary section, in general.

The Used Processing Techniques

A number of procedures were used to detect the expected fault elements along the studied profiles. The processing operations are performed in frequency-domain accomplished by a 2-D Fourier-Transformation of the residual profiles taken from the median-filtered residual gravity map (Figure 12).The used Fourier-Transform edge detection techniques in the current study include; The First and Second Vertical Derivative, Analytical Signal, Tilt Angle and Theta Angle. Most of these methods agree closely in identifying the structural trend and horizontal locations of the causative sources.

1) The First and Second Vertical Derivative (FVD & SVD):

Hood and McClure (1965) first used the first- and second- order vertical derivatives zero points of magnetic anomalies for distinguishing the edge locations of vertical step models. Bhattacharyya (1965) derived the calculation method for the first- and second-order vertical derivatives in the frequency domain. Hood and Teskey (1989) used the first-order vertical derivative zero points for RTP magnetic anomalies to recognize the edge locations of vertical geologic bodies and first used the intersection point of the line connecting maxima and minima and the first-order vertical derivative to accurately determine tilted edges.

The first-order vertical derivative (FVD) of a gravitational anomaly can be expressed as: (df/dz), while the second-order vertical derivative (SVD) of a gravitational anomaly can be expressed as (d^2f/dz^2).

The zero point coordinate location is $x_0 = 0$, located at the edge of the body. Therefore, we can use the zero points to recognize the body's edge location in the thick step model (Verduzco, et al., 2004).

2) The Analytical Signal (AS):

Nabighian (1972) developed the concept of 2-D Analytical Signal, or energy envelope, of potential anomalies. The amplitude (|A|) of the 3-D analytic potential field signal at location (x,y) can be expressed as:

$$AS = \sqrt[2]{\left(\frac{\partial F}{\partial x}\right)^2 + \left(\frac{\partial F}{\partial y}\right)^2 + \left(\frac{\partial F}{\partial z}\right)^2}, \quad \text{..... Equation (1)}$$

AS= |AS(x, y)|, is the amplitude of the analytical signal at (x,y);

F is the original observed gravity field at (x,y).

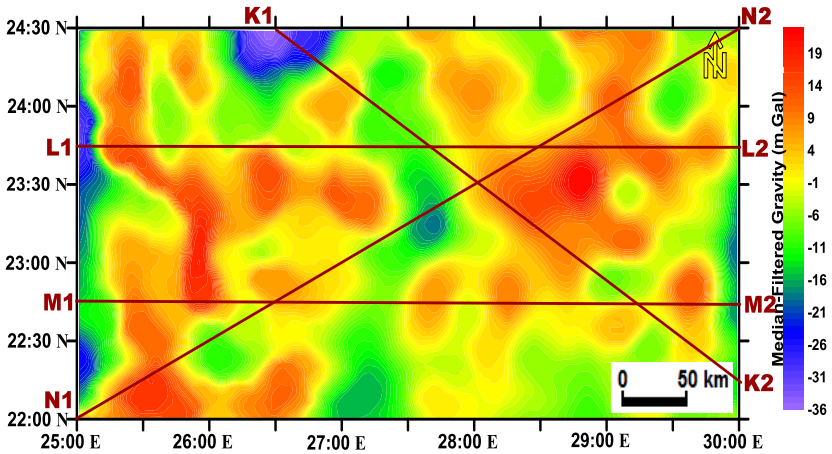

Figure (12) ***Median-Filtered Residual Gravity Map with the studied profiles directions*** **(C.I.=1 m.Gal).**

The amplitude of the analytic signal is a symmetric bell-shaped function (Hsu, et al 1996). By examining its profile across a magnetic source, the analytic signal can be used in interpretation to provide an indication of the edges of the causative body. The maximum value of the analytical signal determines the edges of a gravity body. The analytic signal of gravity anomaly usually enhances the edges of bodies; however, the edges of the deeper bodies might not be recognized clearly.

However, because of the interference effects from different adjacent causative bodies, the use of analytic signal in the 3-D case seems insufficient to detect geologic boundaries. Under these conditions; the detected edges from different bodies are not detachable (Ansari and Alamdar, 2010).

Because the existing interference condition in many cases is not negligible, enhancement of its resolution or using other replacement techniques becomes important. Hsu et al. (1998) defined enhanced analytic signal to reduce the effect of the interference between closely spaced edges and anomalies, which can improve the resolution of the edges effectively.

3) The Tilt Angle (T):

One of the common local phase filters for enhancing features and causative body edge detection in potential field images is the *Tilt Angle*. This filter was first developed by Miller and Singh (1994). Tilt angle is the ratio of the vertical derivative to the absolute amplitude of the total horizontal derivative, which is defined as:

$$T = \tan^{-1}\left(\frac{\partial F/\partial z}{\sqrt{\left(\partial F/\partial x\right)^2+\left(\partial F/\partial y\right)^2}}\right) \qquad \text{Equation (2)}$$

Where, (F) is the magnetic or gravity field. The tilt angle has a range of -90 to +90 degrees and is much simpler to interpret than the analytic signal.

The tilt angle is positive over the source and passes through zero when over or near the edge (where the vertical derivative is zero). The horizontal derivative is maximum and negative outside the source region. In general, the Tilt Angle is maximum and positive at the center of bodies. It is zero at the edges of bodies and negative outside the source regions. However, this filter is not sensitive to the depth of the gravity sources (Ma, and Li, 2012).

***4) The Theta Angle*(θ)**:

The Theta (θ) angle has a range of $0 < \theta < \pi/2$. Although this method restricts the range of angles and we lose information, the result is a well-defined image that is easy to interpret (Wijns et al. 2005).

$$\cos\theta = \left(\frac{\sqrt{\left(\partial F/\partial x\right)^2+\left(\partial F/\partial y\right)^2}}{\sqrt{\left(\partial F/\partial x\right)^2+\left(\partial F/\partial y\right)^2+\left(\partial F/\partial z\right)^2}}\right) \qquad \text{Equation (3)}$$

Equation (3) is the ratio of the magnitudes of the horizontal gradient and the analytic signal, so that the Theta map may also be thought of as a normalization of the horizontal gradient. This normalization introduces an effective gain control, such that the amplitude information is lost, but low-amplitude features are highlighted in a manner similar to automatic gain control maps (e.g., Rajagopalan and Milligan, 1994).

The Theta filter is effective in defining the edges, even if the models are located at different depths. A contact is thus defined in a cos(θ) plot by the pattern of a maximum bracketed by two minima. Furthermore, the minima give an indication both of the depth to the magnetic contact and the direction of dip. The closer the contact is to the surface, the tighter the cos(θ) = [0,1,0] pattern is. The maximum values of the Theta map delineate the spatial location of the edges of the subsurface targets. That means, the edges are located by the cos(θ) Theta's maxima.

For a dipping contact, the minima in the theta profile will be asymmetric because of the distortions in the derivatives of the field. A greater spread between cos(θ) = [0,1] values occurs on the downdip side, increasing with the shallowness of the dip. The point cos(θ) = 1 is also displaced, to a much lesser extent, toward the downdip direction (Thurston and Smith, 1997).

The Results of Processed Data:

The results of the different processing techniques outlined above are represented in the graphs illustrated in Figures 13 and 14. The illustrated graphs were inspected and analyzed visually to follow up the expected structural elements that are probably dissecting the subsurface basement and its overlying sedimentary section. The locations of the deduced structural elements that have common presence within the different used techniques along each of the studied profiles; were compiled and used in the final step of the modeling work of the whole subsurface section along each of the studied four profiles, as shown in Figures (15, 16, 17 and 18).

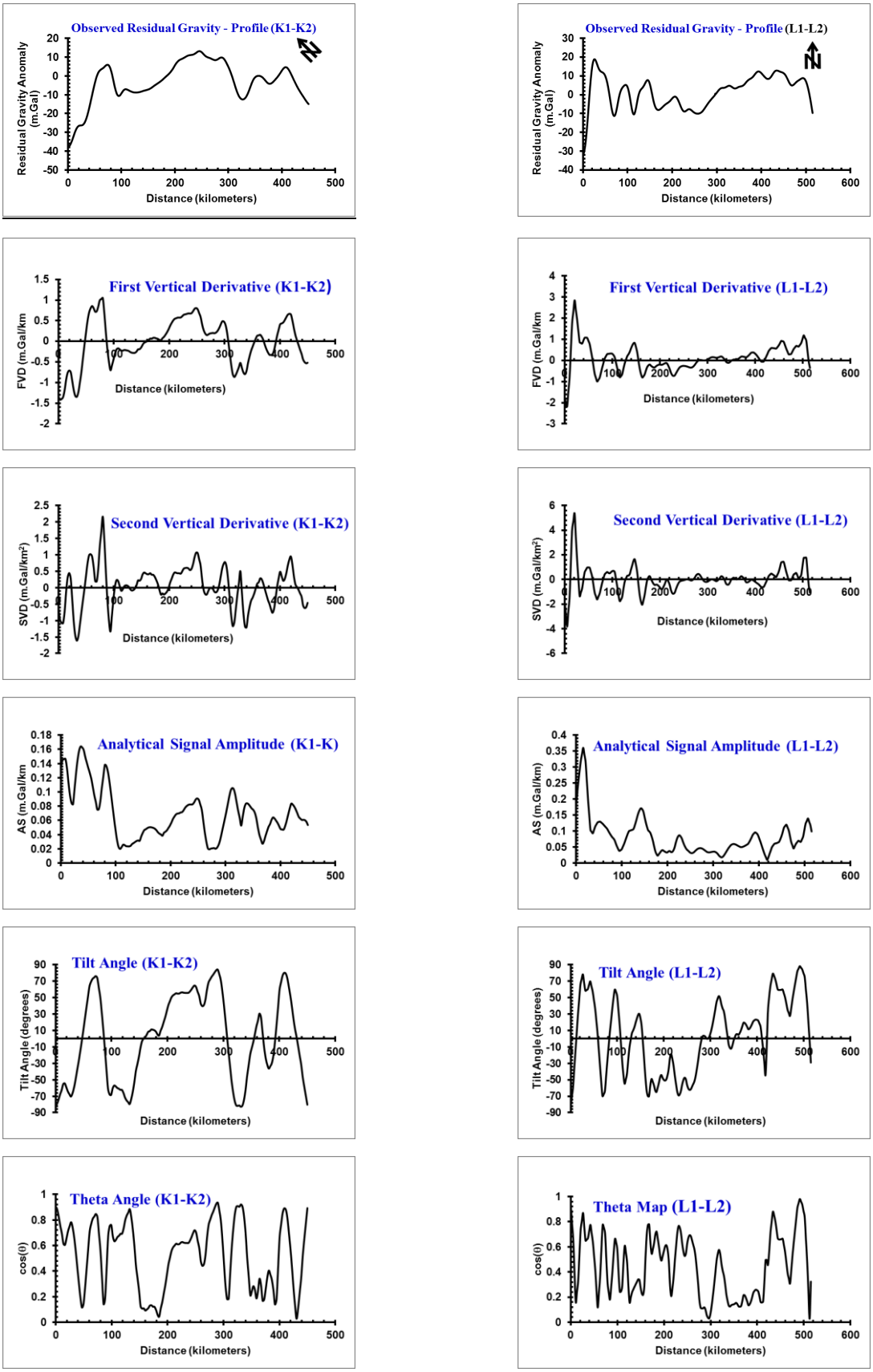

Figure (13): Different processing responses along the Profiles (K1-K2) & (L1-L2).

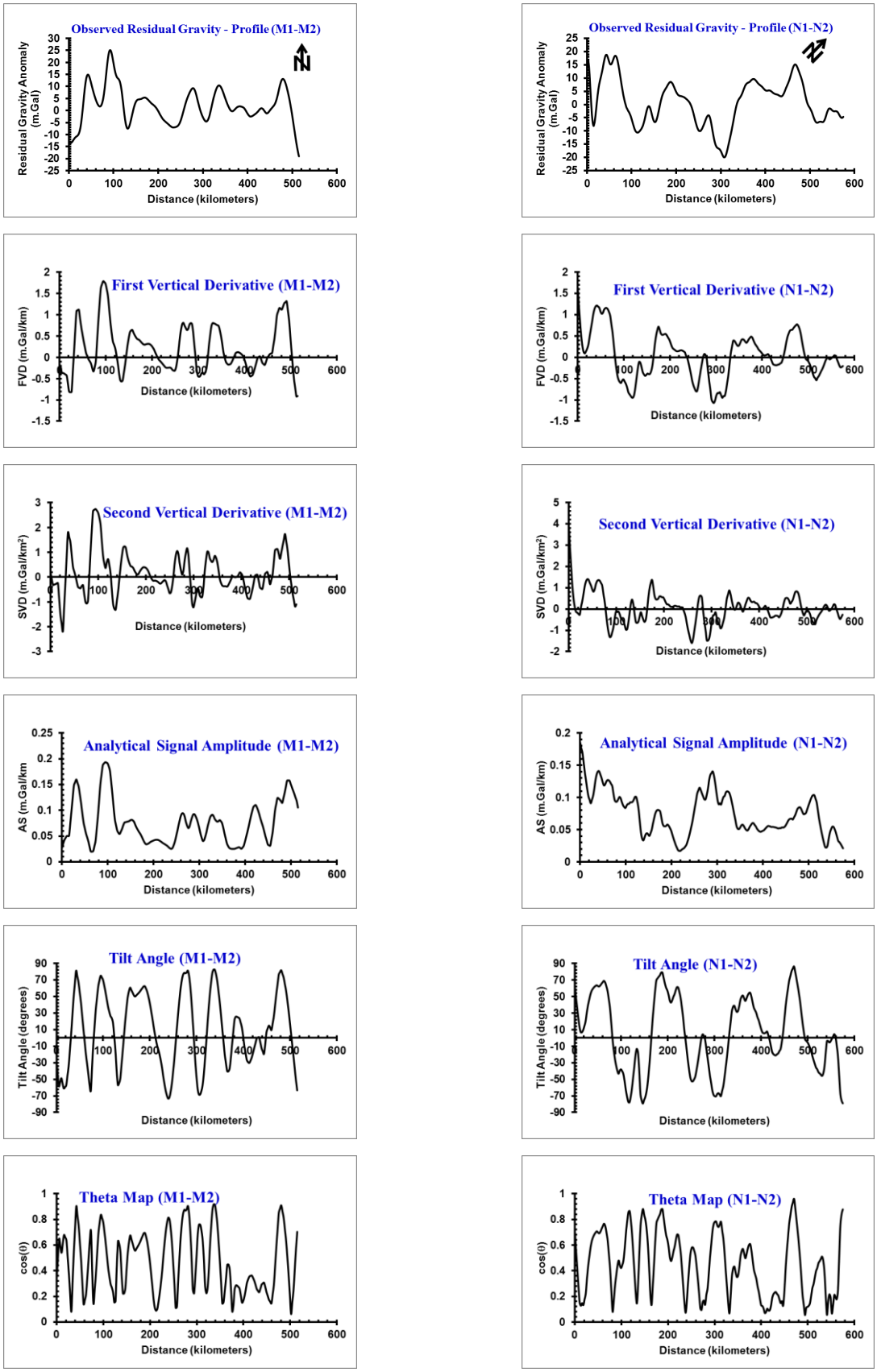

Figure (14): Different processing responses along the Profiles (M1-M2) & (N1-N2).

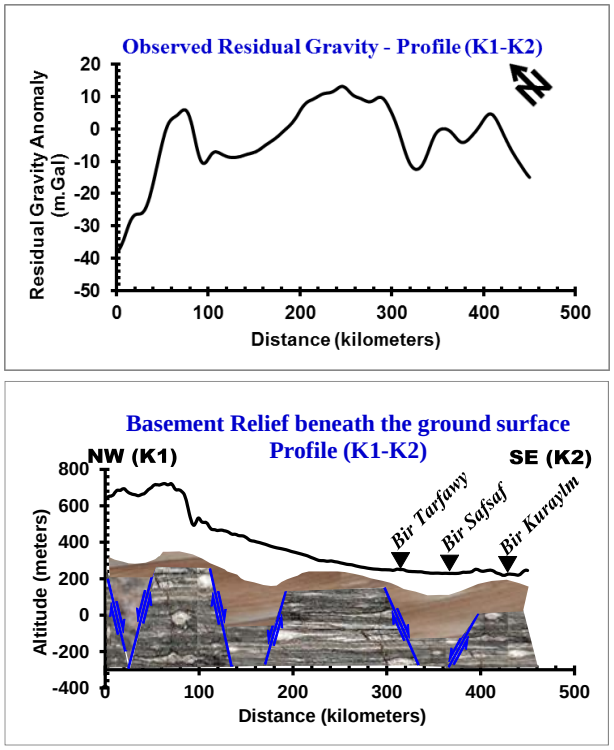

Figure (15): Structural model of the basement surface and the probable affected overlying sedimentary section along the profile K1-K2.

This profile extends about 450 kilometers from its northwestern rim (K1) to its southeastern end (K2) on the median-filtered residual gravity map. The topography along this profile ranges from about 725 meters (asl) at the northwestern side to about 220 meters (asl) at the southeast. The majority of the high elevations are at the northwestern area. The corresponding residual anomaly ranges between -35and 13 m.Gal with local higher and lower anomaly undulations. Several major faults with different fault patterns are responsible for these undulations.

Such anomaly undulations are reflections of the subsurface distribution of basement rocks and their overlying sedimentary section. The interpreted depth of the basement rocks range from about -125 to -520meters below the ground surface, corresponding to depth range of +320 to -190 meters with respect to the mean sea level.

The fault pattern causes such depth variations with three high basement rock blocks (swells) could be interpreted with sub-basins (troughs) in-between of varying subsurface areal extensions. The general dip of the basement surface is towards the southeastern side. Issawi 1971, mentioned that the basement rocks are of Aswan-type granitic nature with gneissic and granodioritic rock. These rocks are overlained by Nubia sequence consists of a succession of sandstone beds with minor intercalation of siltstones, koalinite, and koalinitic sandstone. This is overlained by Quaternary deposits which covers most of the study area and consists of aeolian sands, sand dunes, salt crust, and lake deposits of Pleistocene to Holocene age. Deep graben structure is expected below the province of Bir Tarfawy and Bir Safsaf. Another slightly limited graben structure towards the northwest. Narrower and shallower graben is located at the northwestern rim of the profile.

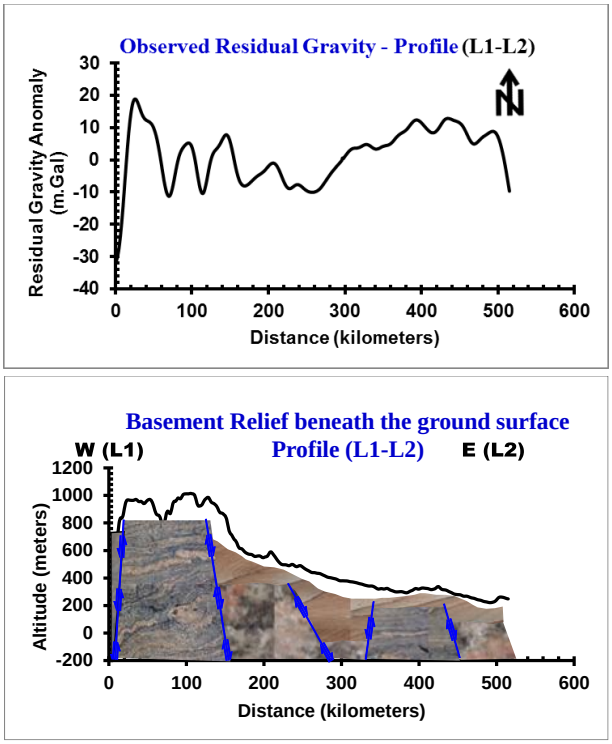

Figure (16): Structural model of the basement surface and the probable affected overlying sedimentary section along the profile L1-L2

This profile runs for about 515 kilometers from its western border (L1) to its eastern side (L2). The topography along this profile ranges from about 1015 meters (asl) at the western side to about 220 meters (asl) at the east. Again, the majority of the high elevations are at the western area. The corresponding residual anomaly ranges between -30 and 13 m.Gal with some local higher and lower anomaly undulations. Shorter wavelength anomalies are at the western half, while wider wavelength anomalies are at the eastern half. Such anomaly undulations are reflections of the subsurface distribution of basement rocks and their overlying sedimentary section. The interpreted depth of the basement rocks range from about -90 to -525 meters below the ground surface, corresponding to depth range of +845 to -125 meters with respect to the mean sea level.

Such depth variations are configuring three high basement blocks could be interpreted with sub-basins in-between of varying subsurface areal extensions. High block of basement rocks is rising up the western side in that area. The general dip of the basement surface is towards the eastern side with same description earlier about basement rocks nature and lithology. These rocks are overlained by Nubia sequence which are .overlained by Quaternary deposits that covers most of the study area of Pleistocene to Holocene age. Deep graben structure is expected at the intersection with longitude 27:30°which reaches a depth of about 125 below mean sea level.

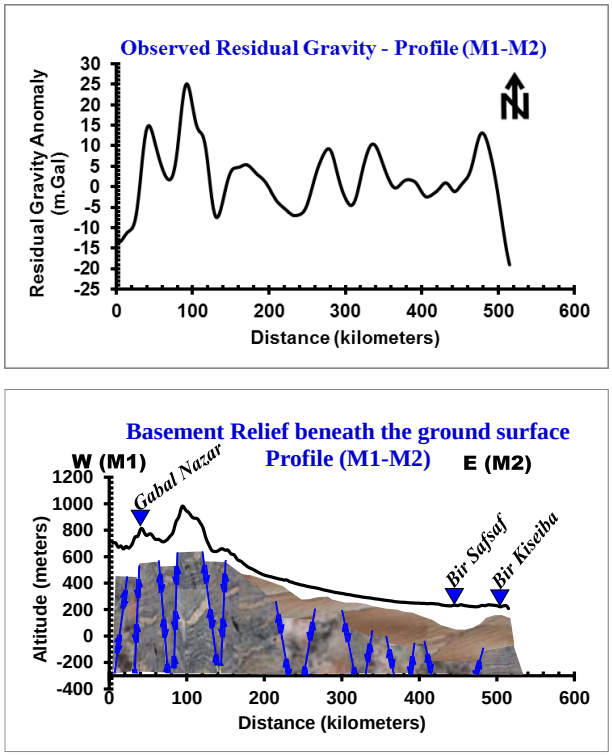

Figure (17): Structural model of the basement surface and the probable affected overlying sedimentary section along the profile M1-M2

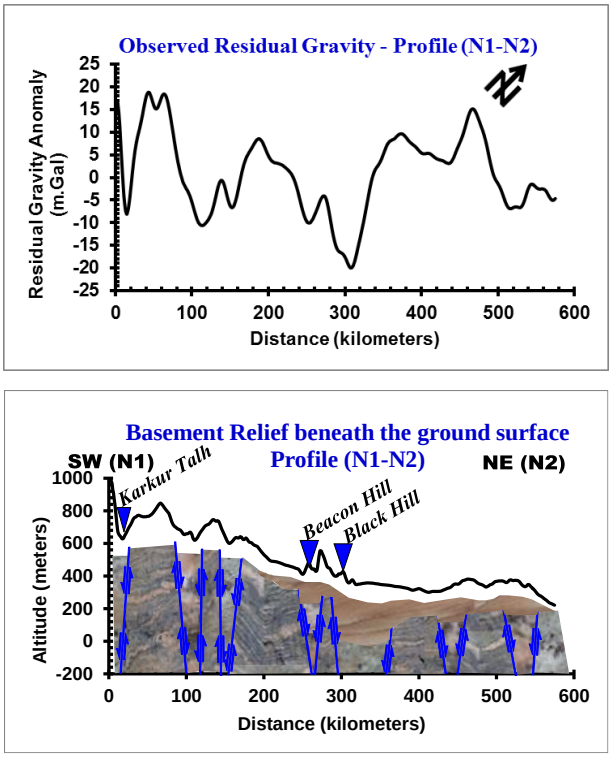

Figure (18): Structural model of the basement surface and the probable affected overlying sedimentary section along the profile N1-N2

This profile runs to the south of profile L1-L2 by about 125 kilometers. It extends for about 515 kilometers from its western border (M1) to its eastern side (M2). The topography along this profile ranges from about 980 to 205 meters towards the east. The corresponding modelled residual anomaly ranges between -16 to+17 m.Gal with some local higher and lower anomaly undulations. The range of variation is smaller than the previous two profiles. This reflects more homogeneity in the subsurface causative sources, even though the interpreted basement depths ranged from -55 to -420 meters below the ground surface. The corresponding depths from mean sea level range from + 650 to -185, as shown in the figure.

There is a general gradient decrease in the basement depth from the West to the East of about 1.5 meter/kilometer. Relatively graben-shaped structure exists below Bir Safsaf area, with an interpreted depth of about 400+ meters.

This profile runs diagonally from the southwestern corner (N1) to the northeastern corner (N2) of the study area. The mapped length of this profile goes for about 575 kilometers. The topography along this profile ranges from about 1010 to 220 meters above mean sea level, with a general gradient decrease of about 1.4 meter/kilometer. This gradient is higher at the southwest and is getting less towards the northeast. The corresponding modelled residual anomaly ranges between -17 to +16m. Gal with some local higher and lower anomaly undulations. The lowest residual gravity value around the middle of the area was interpreted as due to a lowered basin-like graben in the basement surface below the area of ***Black Hill***. Around this area, the basement surface is of shallower interpreted depths. The interpreted basement depths ranged from -80 to -340 meters below the ground surface. The corresponding depths from mean sea level range from +50 to +625, as shown in the figure, where the basement surface is above the mean sea level all along the profile length. Relatively, some basement higher blocks are towards the SW and NE of the study area.

Still the entire area is dominated by the Nubia sequence which is getting thicker underneath the area of Black Hill with relative thinner occurrences elsewhere. This is overlained by thin aeolian sands, sand dunes, and lake deposits of Pleistocene to Holocene age.

SUMMARY AND CONCLUSIONS

First and second vertical derivatives, analytical signal, tilt angle and theta angle as data enhancement were carried out on gravity data for building regional basement structural models. These models detect the major faults along some studied profiles in Owainat and nearby areas, southwestern Egypt.

Data enhancement operations were performed in frequency-domain accomplished by a 2-D Fourier-Transformation of the residual profiles taken from the median-filtered residual gravity map. Most of these operations agree closely in identifying the structural trend and horizontal locations of the causative sources.

Subsurface basement rocks and their overlying sedimentary section are dissected by several major faults with different fault patterns and trends which are responsible for anomaly undulations. Such anomaly undulations are reflections of the variations in both mineral composition and relief of the subsurface basement rocks and their overlying sedimentary section. The fault pattern causes the formation of several swells and troughs of varying subsurface areal extensions in basement rocks. These troughs are contributing together to form a huge basin located in the southeastern part of the study area.

The calculated depth values of the basement rocks are widely variable and ranging from -250 m to 850 m with respect to sea level. The general dip of the basement surface is towards the north, east and northeastern directions.

ACKNOWLEDGMENT

My great appreciation is to the meritorious reviewers together with the Journal Editorial Board for their supportive comments in improving the first version of this manuscript up to its final form.

REFERENCES

Abd El Latif T.A, Mabrouk M.A, and Youssef A.M., (1997): Geoelectrical resistivity survey to delineate the geologic setting of East El-Oweinat area, South Western Desert, Egypt. EGS Proc Ann; 15:45–58

Abdelrahman, E.M., H.M. EI-Araby, T.M. EI-Araby, and E.R. Abo-Ezz (2003): A least-squares derivatives analysis of gravity anomalies due to faulted thin slabs. Geophysics 68 (2), 535-543.

Alexander, M., Prieto, C., Radovich, B., (2003): Basement Structural Analysis Key in Deep Shelf Play. The American oil and gas Reporter, no. 10.

Ansari, A.H. & Alamdar, K. (2010): An improved method for geological boundary detection of potential field anomalies, Journal of Mining and Environment, 2, 37-44.

Beltrao, J.F, Silva J.B.C. and Costa J.C. (1991): Robust polynomial fitting method for regional gravity estimation: Geophysics.doi: 10.1190/ 1.1442960

Bhattacharyya, B.K., (1965): Two-dimensional harmonic analysis as a tool for magnetic interpretation: Geophysics, 30(5), 829 – 857

Burollet, P.F, (1963): Reconnaissance géologique dans le sud-est du bassin de Kufra. Inst. Francais Pétrole 18: 1537-1545.

El Nahry, A.H, Elewa H. H, and Qaddah A.A, (2010): Soil and Groundwater Capability of East Oweinat Area, Western Desert, Egypt Using GIS Spatial Modeling Techniques. Nature and Science. ISSN 2375-7167. 8(8)

El-Baz, F., Boulos, L., Breed, C., Dardir, A., Dowidar, H., El-Etr, H., Embabi, N., Grolier, M., Haynes, V., Ibrahim, M, Issawi, B., Maxwell, T., Mccauley, J., Mchugh, W., Moustafa, A., and Yousif, M., (1978): Journey to the Gilf Kebir and Uweinat, Southwest Egypt. Report.

Gallagher, N.C., and G.L. Wise, (1981): A theoretical analysis of the properties of median filters: IEEE Transactions in Acoustics, Speech and Signal Processing, **29**, 1136–1141. Geophysics, 61, 373-386.

Helaly, A.S. (2018): Mapping the Broad Basement Structural Lineamentsusing the Tilt Angle Derivatives of the Satellite Gravity Data at Oweinat and nearby areas (the Southwestern Desert), EGYPT. Under publication

Hood, P., and McClure, D.J., (1965): Gradient measurements in ground magnetic prospecting: Geophysics. 30(3), 403- 410.

Hood, P.J., Teskey, D.J., (1989): Aeromagnetic gradiometer program of the Geological Survey of Canada. Geophysics 54 (8), 1012–1022.

Hsu, S. K. Sibuet, J.C. & Shyu, C.T. (1996): Depth to magnetic source using generalized analytic signal. Geophysics, Vol. 63, No.6 (November-December 1998); P.1947-1957, 11 Figs.

Hsu, S.K., Coppense, D. & Shyu, C.T. (1998): High resolution detection of geologic boundaries from potential field anomalies: An enhanced analytic signal technique. Geophysics, Vol. 61, No. 2 (March-April 1996); P. 373-386, 9 Figs., 1 Table.

Issawi B. (1971): The geology of Darb E1 Arbain, Western Desert, Egypt. Ann Geol Surv Egypt. ; 1:53-92

Issawi B. (1978): Geology of Nubian West Area, Western Desert, Egypt: Ann. GSE, Cairo. ; 3:237-53.

Justusson, B.I., (1981): Median filtering: Statistical properties, *in* T. S. Huang, ed., Two-dimensional digital signal processing I. Transforms and median filters: Springer-Verlag.

Klitzsch E, Harms J.G, Lejal-Nicol A, List F.K. (1979): Major subdivision and depositional environments of Nubian strata, southwestern Egypt. Bull AAPG; 63 (6):967–74

Klitzsch, E., Lejal-Nicol, A. (1984): Flora and fauna from strata in Southern Egypt and Northern Sudan, Nubian and surrounding areas: Berliner gewiss. Adh., (A), Berlin. ; 50:47-79.

Klitzsch, E. (1984): "Northwestern Sudan and Bordering Areas: Geological Development since Cambrian time", Sonderforschungsbereich 69, Results of Special Research Project Arid Areas, period 1981–1984, Berlin Verlag Von Dietrich Reimer

Klitzsch, E. and Wycisk, P. (1989): Carboniferous of northern Sudan and southern Egypt. XI Congres International de Stratigraphie et de géologie.

Klitzsch, E. and Wycisk, P. (1987): Geology of the sedimentary basin of northern Sudan and bordering areas. Berliner geowissenschaftliche Abhandlungen, A, 75, 1, pp. 97-136, Berlin.

Ma, G., Li, L., (2012): Edge detection in potential fields with the normalized total horizontal derivative. Computers & Geosciences 41 (2012) 83–87.

Mauring, E., and Kihle, O. (2006): Leveling aero-geophysical data using a moving differential median filter. Geophysics, **71**, L5–L11.

Miller, H.G., Singh, V., (1994): Potential field tilt - a new concept for location of potential field sources. Journal of Applied Geophysics 32, 213-217.

Nabighian, M.N., (1972): The analytical signal of 2D magnetic bodies with polygonal cross-section: Its properties and use for automated anomaly interpretation: Geophysics, 37, 507–517.

Nettleton, L.L. (1976): Gravity and Magnetics in Oil Prospecting. McGraw-Hill.

Rajagopalan, S., and P. Milligan, 1994: Image enhancement of aeromagnetic data using automatic gain control: Exploration Geophysics, 25, 173–178.

Said, R., (1962): The geology of Egypt, Elsevier, Amsterdam and New York, (1962), 377 p, Said, R.: New light on the origin of the Qattara Depression. Bull. Soc. Geograph. Egypt, 33, (1960), 37-44.

Stewart, R.R., (1985): Median filtering: Review and a new F/K analogue design: Journal of Canadian Society Exploration Geophysicists, 21, 54–63.

Thurston, J.B., Smith, R.S., (1997): Automatic conversion of magnetic data to depth, dip and susceptibility contrast using the SPI method. Geophysics 62, 807–813.

Verduzco, B., Fairhead, J.D., Green, C.M., (2004): New insights into magnetic derivatives for structural mapping. The Leading Edge 23 (2), 116–119.

Wijns, C., Perez, C., Kowalczyk, P. (2005): Theta map: edge detection in magnetic data. Geophysics 70, 39-43.

APPENDIX (Median Filtering Code): 1)

```
medianfilter.cpp
//   medianfilter.cpp - implementation of
//   1D and 2D median filter routines
//
//   The code is property of LIBROW
//   You can use it on your own
//   When utilizing credit LIBROW site

#include <memory.h>
#include "medianfilter.h"

//   1D MEDIAN FILTER implementation
//     signal - input signal
//     result - output signal
//     N      - length of the signal
void _medianfilter(const element* signal, element* result, int N)
{
  //   Move window through all elements of the signal
  for (int i = 2; i < N - 2; ++i)
  {
    //   Pick up window elements
    element window[5];
    for (int j = 0; j < 5; ++j)
      window[j] = signal[i - 2 + j];
    //   Order elements (only half of them)
    for (int j = 0; j < 3; ++j)
    {
      //   Find position of minimum element
      int min = j;
      for (int k = j + 1; k < 5; ++k)
        if (window[k] < window[min])
          min = k;
      //   Put found minimum element in its place
      const element temp = window[j];
      window[j] = window[min];
      window[min] = temp;
    }
    //   Get result - the middle element
    result[i - 2] = window[2];
  }
}
//   1D MEDIAN FILTER wrapper
//     signal - input signal
//     result - output signal
//     N      - length of the signal
void medianfilter(element* signal, element* result, int N)
{
  //   Check arguments
  if (!signal || N < 1)
    return;
  //   Treat special case N = 1
  if (N == 1)
  {
    if (result)
      result[0] = signal[0];
    return;
  }
  //   Allocate memory for signal extension
  element* extension = new element[N + 4];
  //   Check memory allocation
  if (!extension)
    return;
  //   Create signal extension
  memcpy(extension + 2, signal, N * sizeof(element));
  for (int i = 0; i < 2; ++i)
  {
    extension[i] = signal[1 - i];
    extension[N + 2 + i] = signal[N - 1 - i];
  }
  //   Call median filter implementation
  _medianfilter(extension, result ? result : signal, N + 4);
//   Free memory
    delete[] extension;

//   2D MEDIAN FILTER implementation
//     image  - input image
//     result - output image
//     N      - width of the image
//     M      - height of the image
void _medianfilter(const element* image, element* result, int N, int M)
{
  //   Move window through all elements of the image
  for (int m = 1; m < M - 1; ++m)
    for (int n = 1; n < N - 1; ++n)
    {
      //   Pick up window elements
      int k = 0;
      element window[9];
      for (int j = m - 1; j < m + 2; ++j)
        for (int i = n - 1; i < n + 2; ++i)
          window[k++] = image[j * N + i];
      //   Order elements (only half of them)
      for (int j = 0; j < 5; ++j)
      {
        //   Find position of minimum element
        int min = j;
        for (int l = j + 1; l < 9; ++l)
        if (window[l] < window[min])
          min = l;
        //   Put found minimum element in its place
        const element temp = window[j];
        window[j] = window[min];
        window[min] = temp;
      }
      //   Get result - the middle element
      result[(m - 1) * (N - 2) + n - 1] = window[4];
    }
}
//   2D MEDIAN FILTER wrapper
//     image  - input image
//     result - output image
//     N      - width of the image
//     M      - height of the image
void medianfilter(element* image, element* result, int N, int M)
{
  //   Check arguments
  if (!image || N < 1 || M < 1)
    return;
  //   Allocate memory for signal extension
  element* extension = new element[(N + 2) * (M + 2)];
  //   Check memory allocation
  if (!extension)
    return;
  //   Create image extension
  for (int i = 0; i < M; ++i)
  {
    memcpy(extension + (N + 2) * (i + 1) + 1,
      image + N * i,
      N * sizeof(element));
    extension[(N + 2) * (i + 1)] = image[N * i];
    extension[(N + 2) * (i + 2) - 1] = image[N * (i + 1) - 1];
  }
  //   Fill first line of image extension
  memcpy(extension,
    extension + N + 2,
    (N + 2) * sizeof(element));
  //   Fill last line of image extension
  memcpy(extension + (N + 2) * (M + 1),
    extension + (N + 2) * M,
    (N + 2) * sizeof(element));
  //   Call median filter implementation
  _medianfilter(extension, result ? result : image, N + 2, M + 2);
  //   Free memory
  delete[] extension;
```